Externally Controlled Magnetism and Band Gap in Twisted Bilayer Graphene

A. O. Sboychakov,[1,2] A. V. Rozhkov,[1,2,3] A. L. Rakhmanov,[1,3,2,4] and Franco Nori[1,5]

[1]*Theoretical Quantum Physics Laboratory, RIKEN Cluster for Pioneering Research, Wako-shi, Saitama 351-0198, Japan*
[2]*Institute for Theoretical and Applied Electrodynamics, Russian Academy of Sciences, Moscow, 125412 Russia*
[3]*Moscow Institute for Physics and Technology (State University), Dolgoprudnyi, 141700 Russia*
[4]*Dukhov Research Institute of Automatics, Moscow, 127055 Russia*
[5]*Department of Physics, University of Michigan, Ann Arbor, Michigan 48109-1040, USA*

We theoretically study the effects of electron-electron interaction in twisted bilayer graphene in a transverse dc electric field. When the twist angle is not very small, the electronic spectrum of the bilayer consists of four Dirac cones inherited from each graphene layer. An applied bias voltage leads to the appearance of two holelike and two electronlike Fermi surface sheets with perfect nesting among electron and hole components. Such a band structure is unstable with respect to the exciton band-gap opening due to the screened Coulomb interaction. The exciton order parameter is accompanied by spin-density-wave order. The gap depends on the twist angle and can be varied by a bias voltage. This result correlates well with recent transport measurements [J.-B. Liu *et al.*, Sci. Rep. **5**, 15285 (2015)]. Our proposal allows the coexistence of (i) an externally controlled semiconducting gap and (ii) a nontrivial multicomponent magnetic order. This is interesting for both fundamental research and applications.

Introduction.—A transverse electric field modifies properties of various graphene systems [1]. For example, it opens a gap in the *AB*-bilayer electronic spectrum. The gap is a consequence of the nontrivial chiral structure of the *AB*-bilayer Hamiltonian. Since twisted bilayer graphene (TBLG) [1–12] is in many ways similar to two decoupled graphene sheets, one might naively assume that a transverse bias introduces only minor modifications to the TBLG spectrum. Contrary to this conjecture, our theoretical analysis demonstrates that biased TBLG exhibits unusual features, consistent with recent experiments [13], of interest for both fundamental research and applications. A particularly important aspect of our model is a field-generated multicomponent Fermi surface, with perfect nesting between hole and electron sheets. Interactions destabilize the nested Fermi surface, and the spectrum acquires a gap of exciton origin. The gap is controlled by the applied transverse voltage. Together with the gap, two spin-density-wave (SDW) order parameters, one per graphene valley, appear in the sample. The presence of the magnetic properties distinguishes the biased TBLG from the (magnetically trivial) biased *AB* bilayer. Remarkably, biased TBLG becomes a kind of tunable magnetic semiconductor. The interplay and interference between two SDW orders is an additional intriguing aspect of TBLG. Note that systems with perfect nesting are rare (imperfect or partial nesting is much more common). The realization of such a Fermi surface is of fundamental importance: it allows us to test SDW theories in its simplest setting, without the need for uncontrolled approximations. Furthermore, upon doping, such systems can demonstrate half-metallicity [14]. Currently, many-body properties of *AA*- and *AB*-bilayer graphene [15–23] are actively discussed by theorists, whereas for TBLG this topic is barely touched [24,25]. However, very recent experiments indicate that TBLG hosts interesting many-body phenomena: Mott insulator physics [26] and superconductivity [27] at small twist angles and a tunable semiconducting gap [13] at larger angles. While our formalism cannot describe the small-angle physics [26,27], theoretical conclusions for the higher-angle regime are consistent with experiments [13].

Geometry of twisted bilayer graphene.—A graphene monolayer has a hexagonal crystal structure consisting of two triangular sublattices *A* and *B*. Coordinates of atoms in layer 1 are $\mathbf{r}_\mathbf{n}^{1A} = \mathbf{r}_\mathbf{n}^1 \equiv n\mathbf{a}_1 + m\mathbf{a}_2$ and $\mathbf{r}_\mathbf{n}^{1B} = \mathbf{r}_\mathbf{n}^1 + \boldsymbol{\delta}$, where $\mathbf{n} = (n, m)$ is an integer-valued vector, $\mathbf{a}_{1,2} = a(\sqrt{3}, \mp 1)/2$ are the primitive vectors ($a = 2.46$ Å), and $\boldsymbol{\delta} = a(1/\sqrt{3}, 0)$. Atoms in layer 2 are located at $\mathbf{r}_\mathbf{n}^{2B} = \mathbf{r}_\mathbf{n}^2 \equiv d\mathbf{e}_z + n\mathbf{a}_1' + m\mathbf{a}_2'$ and $\mathbf{r}_\mathbf{n}^{2A} = \mathbf{r}_\mathbf{n}^2 - \boldsymbol{\delta}'$, where $(\mathbf{a}_{1,2}', \boldsymbol{\delta}')$ are the vectors $(\mathbf{a}_{1,2}, \boldsymbol{\delta})$ rotated by an angle θ, and $\mathbf{e}_z$ denotes the unit vector along the z axis. The interlayer distance is $d = 3.35$ Å. The limiting case $\theta = 0$ corresponds to the *AB* stacking. The superstructure exists if $\cos\theta = (3m_0^2 + 3m_0 r + r^2/2)/(3m_0^2 + 3m_0 r + r^2)$, where m_0 and r are coprime positive integers. The number of graphene unit cells inside a supercell is $N_{\text{sc}} = (3m_0^2 + 3m_0 r + r^2)/g$ per layer, where $g = 1$ if $r \neq 3n$, or $g = 3$ otherwise. The number of carbon atoms in the superlattice cell is equal to $4N_{\text{sc}}$.

We introduce $\mathbf{b}_{1,2} = 2\pi(1/\sqrt{3}, \mp 1)/a$, which are the reciprocal lattice vectors for layer 1, and $\mathbf{b}'_{1,2}$ for layer 2 ($\mathbf{b}'_{1,2}$ are θ-rotated $\mathbf{b}_{1,2}$). The vectors $\mathcal{G}_{1,2}$ are the elementary reciprocal vectors for the superlattice. These quantities are related: $\mathbf{b}'_1 = \mathbf{b}_1 + r(\mathcal{G}_1 + \mathcal{G}_2)$ and $\mathbf{b}'_2 = \mathbf{b}_2 - r\mathcal{G}_1$ if $r \neq 3n$, or $\mathbf{b}'_1 = \mathbf{b}_1 + r(\mathcal{G}_1 + 2\mathcal{G}_2)/3$ and $\mathbf{b}'_2 = \mathbf{b}_2 - r(2\mathcal{G}_1 + \mathcal{G}_2)/3$, otherwise. Each graphene layer has two nonequivalent Dirac points located at the corners of its Brillouin zone. Thus, the total number of Dirac points for the bilayer is four. The Brillouin zone of the superlattice is hexagonal shaped. It can be obtained by N_{sc}-times folding [28] of the Brillouin zone of layer 1 or 2. As a result of this folding, Dirac points of each layer are translated to two nonequivalent corners of the reduced Brillouin zone, $\mathbf{K}_1$ and $\mathbf{K}_2$. Points $\mathbf{K}_{1,2}$ can be expressed via vectors $\mathcal{G}_{1,2}$ as $\mathbf{K}_1 = (\mathcal{G}_1 + 2\mathcal{G}_2)/3$ and $\mathbf{K}_2 = (2\mathcal{G}_1 + \mathcal{G}_2)/3$. The Dirac spectrum at $\mathbf{K}_{1,2}$ is doubly degenerate since two nonequivalent Dirac points of constituent layers lie at each corner of the Brillouin zone of the superlattice after the folding. For more details, one may consult Refs. [1,3,29].

Model Hamiltonian.—We investigate the tight-binding model for p_z electrons in undoped TBLG: $\hat{H} = \hat{H}_0 + \hat{H}_{\text{int}}$, where $\hat{H}_0$ is a single-electron Hamiltonian and $\hat{H}_{\text{int}}$ describes electron-electron interaction. Here,

$$\hat{H}_0 = \sum_{\substack{injm \\ ss'\sigma}} t(\mathbf{r}_\mathbf{n}^{is}; \mathbf{r}_\mathbf{m}^{js'}) \hat{d}_{\mathbf{n}is\sigma}^\dagger \hat{d}_{\mathbf{m}js'\sigma} + \frac{V_b}{2} \sum_\mathbf{n} (\hat{n}_{\mathbf{n}1} - \hat{n}_{\mathbf{n}2}), \quad (1)$$

where $\hat{d}_{\mathbf{n}is\sigma}^\dagger$ and $\hat{d}_{\mathbf{n}is\sigma}$ are the creation and annihilation operators of the electron with spin projection σ, located at site $\mathbf{n}$ in the layer i ($=1, 2$) in the sublattice s ($=A, B$), and $\hat{n}_{\mathbf{n}i} = \sum_{s\sigma} \hat{d}_{\mathbf{n}is\sigma}^\dagger \hat{d}_{\mathbf{n}is\sigma}$ is the electron density at the unit cell $\mathbf{n}$ of layer i. For *intralayer* hopping, only the nearest-neighbor term is included. Its amplitude is $-t$, where $t = 2.57$ eV. The *interlayer* hopping is parameterized as described in Refs. [11,12], with the largest interlayer hopping amplitude being equal to $t_0 = 0.4$ eV. The second term in Eq. (1) describes the potential energy difference between layers due to the applied bias voltage V_b. Switching to the momentum representation, one can introduce new single-particle operators $\hat{d}_{\mathbf{p}\mathbf{G}is\sigma} = \mathcal{N}^{-1/2} \sum_\mathbf{n} e^{-i(\mathbf{p}+\mathbf{G})\mathbf{r}_\mathbf{n}^i} \hat{d}_{\mathbf{n}is\sigma}$. Here $\mathcal{N}$ is the number of graphene unit cells in the sample in one layer, the momentum $\mathbf{p}$ lies in the first Brillouin zone of the superlattice, while $\mathbf{G} = m_1 \mathcal{G}_1 + m_2 \mathcal{G}_2$ is the reciprocal vector of the superlattice lying in the first Brillouin zone of the ith layer. The number of such vectors $\mathbf{G}$ is equal to N_{sc} for each graphene layer. Thus, $\hat{H}_0$ becomes

$$\hat{H}_0 = \sum_{\mathbf{p}\sigma} \Bigg(\sum_{\mathbf{G}_1\mathbf{G}_2} \sum_{ijss'} \tilde{t}_{ij}^{ss'}(\mathbf{p}+\mathbf{G}_1; \mathbf{G}_1 - \mathbf{G}_2) \hat{d}_{\mathbf{p}\mathbf{G}_1 is\sigma}^\dagger \hat{d}_{\mathbf{p}\mathbf{G}_2 js'\sigma}$$
$$+ \frac{V_b}{2} \sum_{\mathbf{G}s} (\hat{d}_{\mathbf{p}\mathbf{G}1s\sigma}^\dagger \hat{d}_{\mathbf{p}\mathbf{G}1s\sigma} - \hat{d}_{\mathbf{p}\mathbf{G}2s\sigma}^\dagger \hat{d}_{\mathbf{p}\mathbf{G}2s\sigma}) \Bigg), \quad (2)$$

$$\tilde{t}_{ij}^{ss'}(\mathbf{k}; \mathbf{G}) = \frac{1}{N_{sc}} \sum_\mathbf{nm}' e^{-i\mathbf{k}(\mathbf{r}_\mathbf{n}^i - \mathbf{r}_\mathbf{m}^j)} e^{-i\mathbf{G}\mathbf{r}_\mathbf{m}^j} t(\mathbf{r}_\mathbf{n}^{is}; \mathbf{r}_\mathbf{m}^{js'}). \quad (3)$$

The summation with prime $\sum_\mathbf{nm}'$ denotes that $\mathbf{m}$ runs over sites inside the zeroth supercell, while $\mathbf{n}$ runs over all sites in the sample.

The Hamiltonian (2) can be used to find the single-electron spectrum $E_\mathbf{p}^{(S)}$ and eigenvectors $\Phi_{\mathbf{p}\mathbf{G}is}^{(S)}$, where $S = 1, 2, \ldots, 4N_{sc}$ labels $4N_{sc}$ single-electron bands. The spectrum of (2) is well known. Its part inside the energy window $-0.5t < E < 0.5t$, calculated for $m_0 = 5$, $r = 1$ ($\theta \cong 6.01°$), and $V_b = 0.15t$, is shown in Fig. 1. When $\theta_c < \theta < 60° - \theta_c$ ($\theta_c \cong 1.89°$ for hopping parameters used), the low-energy spectrum consists of four Dirac cones located in pairs at two Dirac points $\mathbf{K}_{1,2}$. Initially, we retain only these four bands, discarding all other electron states. To label the four bands, we will use the symbol $\mathfrak{e}_\mu^w$ ($\mathfrak{h}_\mu^w$) to denote the electron (hole) band of the Dirac cone $\mu = \pm 1$ at the Dirac point $\mathbf{K}_w$, where the valley index is $w = 1, 2$. When $V_b > 0$, the energies of the $\mathfrak{e}_{+1}^w$ and $\mathfrak{h}_{+1}^w$ ($\mathfrak{e}_{-1}^w$ and $\mathfrak{h}_{-1}^w$) bands are shifted to positive (negative) energies. Considering the momentum $\mathbf{p}$ from $\mathbf{K}_w$, we can approximate the electron energy as $E_{\mathbf{p}\mu w}^{\mathfrak{e},\mathfrak{h}} \approx v_F^*(\mu q_F^* \pm |\mathbf{p}|)$, where $v_F^* = v_F^*(\theta)$ is the renormalized Fermi velocity of the TBLG, and $q_F^* \propto V_b/v_F^*$ is the Fermi momentum. Both v_F^* and q_F^* are calculated numerically at half filling. Therefore, if $\hat{\mathfrak{e}}_{\mathbf{k}\mu\sigma}^w$ ($\hat{\mathfrak{h}}_{\mathbf{k}\mu\sigma}^w$) denotes an operator destroying an electron with momentum $\mathbf{k}$ and spin projection σ in the band $\mathfrak{e}_\mu^w$ ($\mathfrak{h}_\mu^w$), the low-energy Hamiltonian becomes

$$\hat{H}_0^{\text{eff}} = v_F^* \sum_{\mathbf{p}\mu w\sigma} [(|\mathbf{p}|+\mu q_F^*)\hat{\mathfrak{e}}_{\mathbf{p}\mu\sigma}^{w\dagger}\hat{\mathfrak{e}}_{\mathbf{p}\mu\sigma}^w - (|\mathbf{p}|-\mu q_F^*)\hat{\mathfrak{h}}_{\mathbf{p}\mu\sigma}^{w\dagger}\hat{\mathfrak{h}}_{\mathbf{p}\mu\sigma}^w].$$

(4)
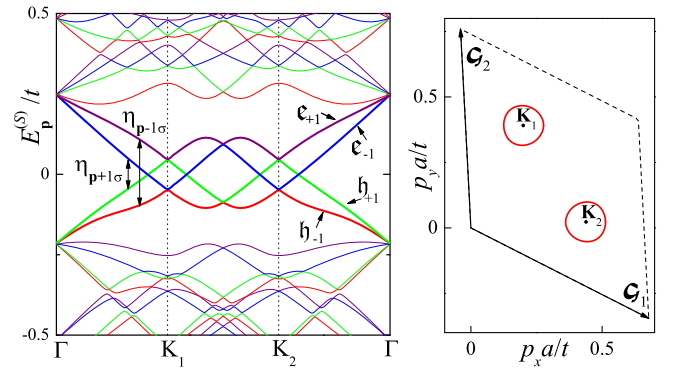
FIG. 1. (Left) Band structure calculated for a sample with $m_0 = 5$, $r = 1$ ($\theta \cong 6.01°$); $V_b = 0.15t/e$. The bands $\mathfrak{e}_\mu$ and $\mathfrak{h}_\mu$ are shown by bold curves. Vertical dashed lines correspond to the Dirac points $\mathbf{K}_{1,2}$. Each vertical double arrow connects two bands forming the anomalous matrix elements $\eta_{\mathbf{p}\pm 1\sigma}$. (Right) The Fermi surface (solid red curves), corresponding to the band structure plotted on the left. A slight trigonal warping of the Fermi lines is seen.

Consequently, two bands, e_{-1}^w and $\mathfrak{h}_{+1}^w$, pass through the Fermi energy (see Fig. 1) and form the Fermi surface (Fermi lines). The Fermi lines may be approximated by two circles $|\mathbf{p}| = q_F^*$ around both Dirac points [30]. The lines are identical for e_{-1}^w and $\mathfrak{h}_{+1}^w$. In the presence of interaction, a nested Fermi surface is unstable with respect to the formation of excitonic order.

To discuss such excitonic order, we need to specify the interaction $\hat{H}_{\text{int}}$,

$$\hat{H}_{\text{int}} = \frac{1}{2} \sum_{\substack{injm \\ ss'\sigma\sigma'}} \hat{d}_{\mathbf{n}is\sigma}^\dagger \hat{d}_{\mathbf{n}is\sigma} U_{ij}(\mathbf{r}_\mathbf{n}^{is} - \mathbf{r}_\mathbf{m}^{js'}) \hat{d}_{\mathbf{m}js'\sigma'}^\dagger \hat{d}_{\mathbf{m}js'\sigma'}. \quad (5)$$

The choice of interaction potential $U_{ij}(\mathbf{r})$ significantly affects the ordered-phase properties. Since the field-induced holes and electrons inhabit different layers, they interact most effectively via the screened Coulomb potential [31,32]. The commonly used Hubbard interaction [20–22,25,33] is quite ineffective in our setting, and we numerically verified [34] that the corresponding corrections are weak. For quasiparticles in the same layer, the Fourier transform of the screened Coulomb potential $U_{ii}(\mathbf{r})$ is $U_{ii}(\mathbf{k}) = v_\mathbf{k} \mathcal{V}_c^{-1}/(1 + \Pi_\mathbf{k} v_\mathbf{k})$. Here, $\mathcal{V}_c = \sqrt{3}a^2/2$ is the graphene unit cell area, the bare Coulomb potential is $v_\mathbf{k} = 2\pi e^2/\epsilon|\mathbf{k}|$, the permittivity of the substrate is ϵ, and $-\Pi_\mathbf{k}$ is the static polarization operator of electrons in the bilayer. When the interacting electrons are in different layers, the corresponding matrix element becomes $U_{12}(\mathbf{k}) = v_\mathbf{k} \mathcal{V}_c^{-1} \exp(-|\mathbf{k}|d)/(1 + \Pi_\mathbf{k} v_\mathbf{k})$.

Once the interaction is specified, the low-energy projection of $\hat{H}_{\text{int}}$ becomes

$$\hat{H}_{\text{int}}^{\text{eff}} = \frac{1}{2\mathcal{N}} \sum_{\mathbf{pq}} \sum_{\mu w} \sum_{\sigma\sigma'} (A_{\mathbf{pq}}^w \hat{\mathfrak{h}}_{\mathbf{p}\mu\sigma}^{w\dagger} \hat{\mathfrak{h}}_{\mathbf{q}\mu\sigma}^w \hat{e}_{\mathbf{q}\bar{\mu}\sigma'}^{w\dagger} \hat{e}_{\mathbf{p}\bar{\mu}\sigma'}^w$$
$$+ B_{\mathbf{pq}}^w \hat{\mathfrak{h}}_{\mathbf{p}\mu\sigma}^{w\dagger} \hat{e}_{\mathbf{q}\bar{\mu}\sigma'}^w \hat{\mathfrak{h}}_{\mathbf{q}\mu\sigma'}^{w\dagger} \hat{e}_{\mathbf{p}\sigma'}^w + \text{H.c.}), \quad (6)$$

where $\bar{\mu} = -\mu$, and $A_{\mathbf{pq}}^w$, $B_{\mathbf{pq}}^w$ are effective coupling constants, obtained by projecting $\hat{H}_{\text{int}}$ in Eq. (5) on the low-energy bands. The procedure is standard, but tedious, and requires both analytical and numerical steps [34]. In (6), we take into account only electron-hole interactions, because these are directly responsible for the gap. Our numerical results demonstrate that, if the momenta $\mathbf{p}$ and $\mathbf{q}$ lay in the w valley (that is, both $\mathbf{p}$ and $\mathbf{q}$ are near the Dirac point $\mathbf{K}_w$), then $A_{\mathbf{pq}}^w \approx \cos^2[(\varphi_\mathbf{p} - \varphi_\mathbf{q})/2] U_{12}(\mathbf{p} - \mathbf{q})$ and $B_{\mathbf{pq}}^w \approx \sin^2[(\varphi_\mathbf{p} - \varphi_\mathbf{q})/2] U_{12}(\mathbf{p} - \mathbf{q})$, where $\varphi_\mathbf{p} = \arctan(p_y/p_x)$ is the polar angle corresponding to $\mathbf{p}$. The deviation from these equalities is larger for smaller θ. Numerical evidence further indicates that the coupling of electron states with different valley indices is negligible. This allows us to keep only the intravalley interaction terms in Eq. (6).

Exciton order parameter.—The interaction (6) binds electrons e and holes $\mathfrak{h}$ into excitons. To describe the exciton condensate we must choose a suitable order parameter. The well-studied AB bilayer, with its variety of orders [15,35–37] offers little guidance here: the AB bilayer has no Fermi surface, and its Hamiltonian possesses a unique chiral structure. Likewise, the knowledge [25] about TBLG ordered phases at low θ is inapplicable: for $\theta < \theta_c$, the single-electron bands are very flat [1,3,11,38] and require a different approach. Of more relevance are the studies of the AA bilayer [20–23,33,39], which has an almost circular nested Fermi surface. With this in mind, we define the following symmetry-breaking expectation values $\eta_{\mathbf{p}\mu\sigma}^w = \langle \hat{\mathfrak{h}}_{\mathbf{p}\mu\sigma}^{w\dagger} \hat{e}_{\mathbf{p}\bar{\mu}\bar{\sigma}}^w \rangle$, where $\bar{\sigma}$ means "not σ". An order parameter $\langle \hat{\mathfrak{h}}_{\mathbf{p}\mu\sigma}^{w\dagger} \hat{e}_{\mathbf{p}\bar{\mu}\bar{\sigma}}^{w'} \rangle$, coupling valleys w and w', is not supported by our interaction if $w \neq w'$. Thus, the valley index may be suppressed. This ordered phase is the planar SDW. Its magnetic moments are localized on the links connecting atoms in different layers. Since the nesting vector is zero, the SDW period coincides with the superstructure periodicity. Observable magnetic moments distribution depends on the interference of the order parameters in different valleys, which presented formalism cannot capture. Finally, the charge-density-wave order $\sum_\sigma \langle \hat{\mathfrak{h}}_{\mathbf{p}\mu\sigma}^{w\dagger} \hat{e}_{\mathbf{p}\bar{\mu}\sigma}^w \rangle$ is energetically unfavorable in comparison to the SDW one, as it can be seen from Hamiltonian (6). Using the η's, we can decouple $H_{\text{int}}^{\text{eff}}$. The resultant mean-field Hamiltonian becomes quadratic in $\hat{e}$ and $\hat{\mathfrak{h}}$. It can be expressed as $\hat{H}_{\text{MF}} = \sum_{\mathbf{p}\mu} \hat{\Psi}_{\mathbf{p}\mu}^\dagger H_{\mathbf{p}\mu} \hat{\Psi}_{\mathbf{p}\mu}$, where $\hat{\Psi}_{\mathbf{p}\mu} = (\hat{\mathfrak{h}}_{\mathbf{p}\mu\uparrow}, \hat{e}_{\mathbf{p}\bar{\mu}\uparrow}, \hat{\mathfrak{h}}_{\mathbf{p}\mu\downarrow}, \hat{e}_{\mathbf{p}\bar{\mu}\downarrow})^T$, and

$$H_{\mathbf{p}\mu} = \begin{pmatrix} E_{\mathbf{p}\mu}^\mathfrak{h} & 0 & 0 & -\Delta_{\mathbf{p}\mu\uparrow}^* \\ 0 & E_{\mathbf{p}\bar{\mu}}^e & -\Delta_{\mathbf{p}\mu\downarrow} & 0 \\ 0 & -\Delta_{\mathbf{p}\mu\downarrow}^* & E_{\mathbf{p}\mu}^\mathfrak{h} & 0 \\ -\Delta_{\mathbf{p}\mu\uparrow} & 0 & 0 & E_{\mathbf{p}\bar{\mu}}^e \end{pmatrix}. \quad (7)$$

Here the order parameter is defined as $\Delta_{\mathbf{p}\mu\sigma} = \mathcal{N}^{-1} \sum_\mathbf{q} [A_{\mathbf{pq}}\eta_{\mathbf{q}\mu\sigma} + B_{\mathbf{pq}}\eta_{\mathbf{q}\bar{\mu}\bar{\sigma}}^*]$. Minimizing the total energy at zero temperature and at half filling, we obtain the system of equations for the order parameters

$$\Delta_{\mathbf{p}\mu} = \frac{\mathcal{V}_c}{2} \int \frac{d^2 q}{(2\pi)^2} \left(\frac{A_{\mathbf{pq}}\Delta_{\mathbf{q}\mu}}{\sqrt{\Delta_{\mathbf{q}\mu}^2 + E_{\mathbf{q}\mu}^2}} + \frac{B_{\mathbf{pq}}\Delta_{\mathbf{q}\bar{\mu}}}{\sqrt{\Delta_{\mathbf{q}\bar{\mu}}^2 + E_{\mathbf{q}\bar{\mu}}^2}} \right), \quad (8)$$

where we assume that $\Delta_{\mathbf{p}\mu\uparrow} = \Delta_{\mathbf{p}\mu\downarrow} \equiv \Delta_{\mathbf{p}\mu} = \Delta_{\mathbf{p}\mu}^*$, the integration is performed over the Brillouin zone of the superlattice, and $E_{\mathbf{q}\mu} = [E_{\mathbf{q}\bar{\mu}}^e - E_{\mathbf{q}\mu}^\mathfrak{h}]/2$. If $\Delta_{\mathbf{p}+1} \to 0$, the right-hand side of Eq. (8) acquires a logarithmic singularity, implying that the studied instability is driven by $\Delta_{\mathbf{p}+1}$. Its value at the Fermi surface gives us the energy

gap. As for $\Delta_{\mathbf{p}-1}$, its role is to renormalize the strength of the symmetry breaking and it cannot be neglected in the numerical calculations.

Solving (8), several simplifications are made. First, we approximate the Fermi surface by a circle of radius q_F^*. The functions $A_{\mathbf{pq}}$ and $B_{\mathbf{pq}}$ are replaced by constants $\bar{A}$ and $\bar{B}$, obtained by averaging $A_{\mathbf{pq}}$ and $B_{\mathbf{pq}}$ over the Fermi surface. The $\mathbf{p}$ dependence of $\Delta_{\mathbf{p}\mu}$ is simplified: $\Delta_{\mathbf{p}\mu} = \Delta_\mu \Theta(q_\Lambda - |p - q_F^*|)$, where $q_\Lambda > 0$ is the cutoff momentum of the interaction and $\Theta(q)$ is the step function. The cutoff value can be found [31,32] by the requirement $U_{12}(q_\Lambda) = U_{12}(0)/2$. Assuming that $q_\Lambda d \ll 1$ (which is valid for $V_b \lesssim t_0$ and $e^2/\epsilon v_F \lesssim 1$), we derive $q_\Lambda \approx 2\pi\alpha v_F \Pi_0$, where $\alpha = e^2/\epsilon v_F$ is the graphene fine structure constant and $v_F = at\sqrt{3}/2$ is the Fermi velocity of single-layer graphene. Finally, since in the long-wavelength limit ($|\mathbf{k}| \ll |\mathbf{b}_{1,2}|$), the function $\Pi_{\mathbf{k}}$ is equal to the density of states (DOS) at the Fermi level: $\Pi_{\mathbf{k}} \approx \Pi_0 \approx 4q_F^*/(\pi v_F^*)$, and $q_\Lambda = 8\alpha(v_F/v_F^*)q_F^*$.

Approximate solution, weak-interaction limit.—In the weak-interaction limit, $\alpha \to 0$, only the states with small momenta $q = |\mathbf{q}| \ll |\mathbf{G}_{1,2}|$ are important. For these

$$E_{\mathbf{q}\mu} \approx v_F^*(|\mathbf{q}| - \mu q_F^*). \qquad (9)$$

In this regime, the region of integration in Eq. (8) becomes a ring or a circle centered at the Dirac point, defined by $q_1 < |\mathbf{q}| < q_2$, where $q_1 = \max[0, q_F^* - q_\Lambda]$ and $q_2 = q_F^* + q_\Lambda$. Therefore, the system (8) becomes

$$
\Delta_\mu = \frac{1}{2}\int_{q_1}^{q_2} dq \left[\frac{q\lambda_A \Delta_\mu}{\sqrt{\Delta_\mu^2 + v_F^{*2}(q - \mu q_F^*)^2}} \right.
$$
$$
\left. + \frac{q\lambda_B \Delta_{\bar{\mu}}}{\sqrt{\Delta_{\bar{\mu}}^2 + v_F^{*2}(q + \mu q_F^*)^2}} \right], \qquad \mu = \pm 1, \quad (10)
$$

where $\lambda_A = \mathcal{V}_c \bar{A}/(2\pi)$, $\lambda_B = \mathcal{V}_c \bar{B}/(2\pi)$. Assuming that $q_\lambda \ll q_F^*$ and $\Delta_\mu \ll V_b$, we solve system (10) analytically,

$$\Delta_+ \approx 2v_F q_F^* \alpha \exp\{-1/\Lambda + 4\alpha^*\}, \qquad \Delta_- = \frac{\bar{B}}{\bar{A}}\Delta_+, \qquad (11)$$

where $\alpha^* = e^2/(\epsilon v_F^*)$ is the "renormalized α" and $\Lambda \approx \lambda_A q_F^*/v_F^*$. The solution (11) for Δ_+ has a BCS-like structure, which dictates a high sensitivity of the gap Δ_+ to the effective interaction strength $\bar{A}$.

Approximate solution, strong-interaction limit.—The solution (11) is valid when $\alpha \ll 1$. Estimates show, however, that for a suspended bilayer $\alpha \approx 2.6$. When α increases, the cutoff q_Λ can exceed the size of the super-lattice Brillouin zone. In this case, we should take into account more bands in the Hamiltonians (4) and (6) and,
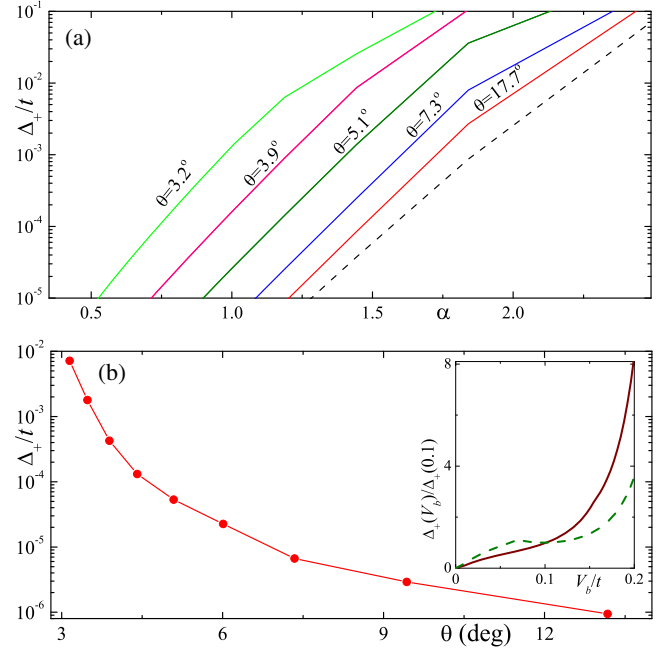
FIG. 2. (a) Solid curves show the gap Δ_+ versus α for superstructures with $r = 1$ and $m_0 = 2, 4, 6, 8, 10$ (twist angles $\theta \cong 17.7, 7.3, 5.1, 3.9, 3.2$ deg) for $V_b/t = 0.1$. The dashed curve corresponds to the decoupled ($t_0 = 0$) graphene layers. In this case, the function $\Delta_+(\alpha)$ is almost independent of θ. (b) Δ_+ versus θ calculated for $V_b/t = 0.037$ and $\alpha = 1.044$. The inset shows Δ_+ versus V_b for $\alpha = 0.306$ (solid curve) and for $\alpha = 0.719$ (dashed curve) calculated for the superstructure $m_0 = 5$, $r = 1$.

consequently, introduce additional order parameters $\Delta_{\mathbf{p}\mu}$. This makes the formalism quite involved. A simpler approach is to neglect the fine structure of the high-energy ($|\mathbf{q}| > |\mathcal{G}_{1,2}|$) single-electron states and treat them as if there is no hopping between the layers. Such a layer decoupling is justified [40] if $\theta > \theta_c$. For example, the high-energy DOS of TBLG is well approximated by the single-layer DOS (see Fig. 7 of Ref. [41]). This simplification allow us to extend the upper integration limit q_2 in (10) to $\sim q_\Lambda < |\mathbf{b}_{1,2}|$. Note that, in the interval $|\mathcal{G}_1|/(2\sqrt{3}) < q < q_\Lambda$, because of the decoupling, the velocity v_F^* in (10) must be replaced by v_F. Finally, even at large q_Λ, we may study each valley $\mathbf{K}_{1,2}$ separately [34]. This is a consequence of the decoupling of the layers.

Results and Discussion.—We numerically solved the system (10), valid in the weak-interaction limit. We also solved its modified version suitable for the strong-interaction regime. The computations were performed for several superstructures with $r = 1$ in a wide range of values for V_b and α. Major results of our study are presented in Fig. 2, where Δ_+ is plotted for different model parameters. (We focus on Δ_+, since it provides the electron energy gap, a quantity of crucial importance for the system properties.) The gap strongly (exponentially) depends on the interaction

strength for all superstructures; see Fig. 2(a). The gap is appreciable when $\alpha \gtrsim 1 \Leftrightarrow \epsilon \lesssim 2.5$ (note that the ratio $\Delta_+/t \sim 10^{-2}$ corresponds to $\Delta_+ \sim 300$ K). Thus, to observe the gap at room temperatures [42], the permittivity of the substrate should not be large. The data in Fig. 2(a) imply that for any α, the gap is larger for smaller twist angles. This point is illustrated in Fig. 2(b), where Δ_+ is plotted versus θ for fixed α and V_b. We note that the band gap increases by about 4 orders of magnitude, when the twist angle changes from $\theta \cong 17.7°$ to $\theta \cong 3.2°$. Such a strong enhancement can be explained by the reduction of the Fermi velocity due to the interlayer hybridization.

The graph in the inset shows the gap versus the bias voltage for weak and moderate α. This dependence is linear at small V_b, in agreement with (11). Indeed, because of screening, the interaction parameter $\bar{A}$ is proportional to $1/q_F^*$ at weak bias; therefore, the dimensionless parameter $\Lambda \sim \bar{A}q_F^*$ is insensitive to V_b and only the preexponential factor in (11) linearly depends on V_b. At strong interaction, the function $\Delta_+(V_b)$ can be nonmonotonic for large bias voltages. Thus, our findings demonstrate that the TBLG may serve as a system with a tunable insulating gap. Recently, experimental evidence in favor of such a gap was reported [13].

In conclusion, we demonstrated that biased TBLG can become a magnetic semiconductor with tunable gap, whose value, depending on parameters, can be as large as several hundreds Kelvin. The gapful state is an exciton insulator, accompanied by SDW order. The insulator is stabilized due to perfect nesting of the field-generated Fermi surface. These results have both fundamental and applied significance.

[1] A. Rozhkov, A. Sboychakov, A. Rakhmanov, and F. Nori, Electronic properties of graphene-based bilayer systems, Phys. Rep. 648, 1 (2016).

[2] J. M. B. Lopes dos Santos, N. M. R. Peres, and A. H. Castro Neto, Graphene Bilayer with a Twist: Electronic Structure, Phys. Rev. Lett. 99, 256802 (2007).

[3] J. M. B. Lopes dos Santos, N. M. R. Peres, and A. H. Castro Neto, Continuum model of the twisted graphene bilayer, Phys. Rev. B 86, 155449 (2012).

[4] R. Bistritzer and A. H. MacDonald, Moiré bands in twisted double-layer graphene, Proc. Natl. Acad. Sci. U.S.A. 108, 12233 (2011).

[5] S. Shallcross, S. Sharma, and O. A. Pankratov, Twist boundary in graphene: Energetics and electric field effect, J. Phys. Condens. Matter 20, 454224 (2008).

[6] S. Shallcross, S. Sharma, and O. A. Pankratov, Quantum Interference at the Twist Boundary in Graphene, Phys. Rev. Lett. 101, 056803 (2008).

[7] E. J. Mele, Commensuration and interlayer coherence in twisted bilayer graphene, Phys. Rev. B 81, 161405 (2010).

[8] S. Shallcross, S. Sharma, E. Kandelaki, and O. A. Pankratov, Electronic structure of turbostratic graphene, Phys. Rev. B 81, 165105 (2010).

[9] R. de Gail, M. O. Goerbig, F. Guinea, G. Montambaux, and A. H. Castro Neto, Topologically protected zero modes in twisted bilayer graphene, Phys. Rev. B 84, 045436 (2011).

[10] E. J. Mele, Band symmetries and singularities in twisted multilayer graphene, Phys. Rev. B 84, 235439 (2011).

[11] A. O. Sboychakov, A. L. Rakhmanov, A. V. Rozhkov, and F. Nori, Electronic spectrum of twisted bilayer graphene, Phys. Rev. B 92, 075402 (2015).

[12] A. V Rozhkov, A. O Sboychakov, A. L Rakhmanov, and F. Nori, Single-electron gap in the spectrum of twisted bilayer graphene, Phys. Rev. B 95, 045119 (2017).

[13] J.-B. Liu, P.-J. Li, Y.-F. Chen, Z.-G. Wang, F. Qi, J.-R. He, B.-J. Zheng, J.-H. Zhou, W.-L. Zhang, L. Gu et al., Observation of tunable electrical bandgap in large-area twisted bilayer graphene synthesized by chemical vapor deposition, Sci. Rep. 5, 15285 (2015).

[14] A. V. Rozhkov, A. L. Rakhmanov, A. O. Sboychakov, K. I. Kugel, and F. Nori, Spin-Valley Half-Metal as a Prospective Material for Spin Valleytronics, Phys. Rev. Lett. 119, 107601 (2017).

[15] O. Vafek and K. Yang, Many-body instability of Coulomb interacting bilayer graphene: Renormalization group approach, Phys. Rev. B 81, 041401 (2010).

[16] R. Nandkishore and L. Levitov, Quantum anomalous Hall state in bilayer graphene, Phys. Rev. B 82, 115124 (2010).

[17] R. Nandkishore and L. Levitov, Dynamical Screening and Excitonic Instability in Bilayer Graphene, Phys. Rev. Lett. 104, 156803 (2010).

[18] J. Nilsson, A. H. Castro Neto, N. M. R. Peres, and F. Guinea, Electron-electron interactions and the phase diagram of a graphene bilayer, Phys. Rev. B 73, 214418 (2006).

[19] Y. Wang, H. Wang, J.-H. Gao, and F.-C. Zhang, Layer antiferromagnetic state in bilayer graphene: A first-principles investigation, Phys. Rev. B 87, 195413 (2013).

[20] A. L. Rakhmanov, A. V. Rozhkov, A. O. Sboychakov, and F. Nori, Instabilities of the AA-Stacked Graphene Bilayer, Phys. Rev. Lett. 109, 206801 (2012).

[21] A. O. Sboychakov, A. V. Rozhkov, A. L. Rakhmanov, and F. Nori, Antiferromagnetic states and phase separation in doped AA-stacked graphene bilayers, Phys. Rev. B 88, 045409 (2013).

[22] R. S. Akzyanov, A. O. Sboychakov, A. V. Rozhkov, A. L. Rakhmanov, and F. Nori, AA-stacked bilayer graphene in an applied electric field: Tunable antiferromagnetism and coexisting exciton order parameter, Phys. Rev. B 90, 155415 (2014).

[23] D. S. de la Peña, M. M. Scherer, and C. Honerkamp, Electronic instabilities of the AA-honeycomb bilayer, Ann. Phys. (Amsterdam) **526,** 366 (2014).

[24] J. González, Magnetic and Kohn-Luttinger instabilities near a Van Hove singularity: Monolayer versus twisted bilayer graphene, Phys. Rev. B **88,** 125434 (2013).

[25] L. A. Gonzalez-Arraga, J. L. Lado, F. Guinea, and P. San-Jose, Electrically Controllable Magnetism in Twisted Bilayer Graphene, Phys. Rev. Lett. **119,** 107201 (2017).

[26] Y. Cao, V. Fatemi, A. Demir, S. Fang, S. L. Tomarken, J. Y. Luo, J. D. Sanchez-Yamagishi, K. Watanabe, T. Taniguchi, E. Kaxiras *et al.*, Correlated insulator behaviour at half-filling in magic-angle graphene superlattices, Nature (London) **556,** 80 (2018).

[27] Y. Cao, V. Fatemi, S. Fang, K. Watanabe, T. Taniguchi, E. Kaxiras, and P. Jarillo-Herrero, Unconventional superconductivity in magic-angle graphene superlattices, Nature (London) **556,** 43 (2018).

[28] H. Nishi, Y.-i. Matsushita, and A. Oshiyama, Band-unfolding approach to Moiré-induced band-gap opening and Fermi level velocity reduction in twisted bilayer graphene, Phys. Rev. B **95,** 085420 (2017).

[29] E. J. Mele, Interlayer coupling in rotationally faulted multilayer graphenes, J. Phys. D **45,** 154004 (2012).

[30] Fermi lines are nearly circular when the bias voltage is small enough, while trigonal warping reveals itself at larger V_b (see Fig. 1). The trigonal warping becomes more pronounced for superstructures with smaller θ. Nevertheless, trigonal warping does not destroy the ideal nesting of Fermi surfaces.

[31] Y. E. Lozovik and A. Sokolik, Electron-hole pair condensation in a graphene bilayer, JETP Lett. **87,** 55 (2008).

[32] Y. E. Lozovik and A. Sokolik, Multi-band pairing of ultra-relativistic electrons and holes in graphene bilayer, Phys. Lett. A **374,** 326 (2009).

[33] A. O. Sboychakov, A. L. Rakhmanov, A. V. Rozhkov, and F. Nori, Metal-insulator transition and phase separation in doped AA-stacked graphene bilayer, Phys. Rev. B **87,** 121401 (2013).

[34] For details, see Supplemental Material at http://link.aps.org/supplemental/10.1103/PhysRevLett.120.266402, which includes Refs. [2–4,11,28,31,32].

[35] Y. Lemonik, I. Aleiner, and V. I. Fal'ko, Competing nematic, antiferromagnetic, and spin-flux orders in the ground state of bilayer graphene, Phys. Rev. B **85,** 245451 (2012).

[36] F. Zhang and A. H. MacDonald, Distinguishing Spontaneous Quantum Hall States in Bilayer Graphene, Phys. Rev. Lett. **108,** 186804 (2012).

[37] M. Kharitonov, Canted Antiferromagnetic Phase of the $\nu = 0$ Quantum Hall State in Bilayer Graphene, Phys. Rev. Lett. **109,** 046803 (2012).

[38] P. San-Jose and E. Prada, Helical networks in twisted bilayer graphene under interlayer bias, Phys. Rev. B **88,** 121408 (2013).

[39] L. Brey and H. A. Fertig, Gapped phase in *AA*-stacked bilayer graphene, Phys. Rev. B **87,** 115411 (2013).

[40] Modifications in the single-particle dispersion of the TBLG are the strongest for energies ε below the first van Hove singularity: $|\varepsilon| < E_{\mathrm{vH}}^{(1)}$. Both the van Hove singularity and low-energy renormalizations are due to interlayer hybridization amplitudes $\tilde{t}_{12}^{ss'}(\mathbf{k};\mathbf{G})$, where $\mathbf{G}$ is either 0, $-\mathcal{G}_1$, or $\mathcal{G}_2$ [3]. At $|\varepsilon| > E_{\mathrm{vH}}^{(1)}$, the interlayer tunneling is controlled by higher values of momentum $\mathbf{G}$. It is known [2,3] that $\tilde{t}_{12}^{ss'}(\mathbf{k};\mathbf{G})$ quickly decays when $|\mathbf{G}|$ grows. Thus, we neglect the interlayer tunneling at $|\mathbf{G}| > |\mathcal{G}_{1,2}|$ and approximate high-energy bilayer states by the wave functions localized inside an individual layer.

[41] S. Shallcross, S. Sharma, and O. Pankratov, Emergent momentum scale, localization, and van Hove singularities in the graphene twist bilayer, Phys. Rev. B **87,** 245403 (2013).

[42] Being a 2D material, TBLG does not possess a long-range order at finite temperatures. However, one can expect that the short-range order will survive up to temperatures about the value of the gap Δ_+ at zero temperature. For graphene systems, this has been shown for *AA*-stacked bilayer graphene in Ref. [21]. However, the TBLG has a superlattice, and the size of its supercell can be substantially large. The effects of fluctuations in this case require a separate study.